Research Article Vol. 56, No. 36 / December 20 2017 / Applied Optics 10009

applied optics

Performance improvement of the Giant Steerable Science Mirror prototype: calibration, added-on damping treatment, and warping harness

Qi-chang An,[1,2] Jing-xu Zhang,[1] Fei Yang,[1] Hong-chao Zhao,[1] and Liang Wang[1,*]

[1]Changchun Institute of Optics, Fine Mechanics and Physics, Chinese Academy of Sciences, Changchun 130033, China
[2]University of Chinese Academy of Sciences, Beijing 100039, China
*Corresponding author: wangliang.ciomp@foxmail.com

Received 22 September 2017; revised 16 November 2017; accepted 19 November 2017; posted 21 November 2017 (Doc. ID 307736); published 14 December 2017

The Giant Steerable Science Mirror (GSSM), the tertiary mirror of the Thirty Meter Telescope, is designed to meet complicated requirements. Calibration, added-on damping treatment, and warping harness will lower the cost to meet those strict requirements. A laser tracker and sphere-mounted retro-reflector (SMR) were used to calibrate the GSSM prototype (GSSMP). Use of non-uniform distribution SMRs will lower the systematic metrology error. The frequency response function between input excitation and dummy mirror responses is investigated to realize the design of tuned mass damping, which will be added on the GSSMP as a damping treatment to improve settling time and tracing performance. Finally, we utilized the warping harness, combining Zernike mode and bending mode, to relax the requirements of GSSM for low-order mirror figure aberrations.

OCIS codes: (120.4640) Optical instruments; (120.4610) Optical fabrication; (120.4800) Optical standards and testing; (120.5050) Phase measurement.

https://doi.org/10.1364/AO.56.010009

1. INTRODUCTION

The Thirty Meter Telescope (TMT) is a future large telescope, whose tertiary mirror is noted as the Giant Steerable Science Mirror (GSSM), the largest planar mirror (3.594 m × 2.536 m) in the world. Different from other steering mirrors, light transmission from the primary mirror to instruments will be realized by GSSM. What is more, the performance of GSSM is under high requirements, which is hard to reach only by design. Thus, we illustrate three coherent procedures, including calibration, added-on damping treatment, and warping harness, to obtain a high-quality GSSM.

Calibration is aimed at meeting the special requirements and removing undesired systematic effects from measurement. Calibration, making GSSM perform to accuracy that is otherwise impossible or very expensive to achieve, has been widely used in the TMT primary mirror assembly (M1 structural deformation due to gravity, M1 structural deformation due to temperature, azimuth, and elevation tape encoder errors, etc.). The alignment and phasing system (APS) effectively calibrates the M1 edge sensors to realize alignment and phasing, so that the telescope will be able to perform well at diffraction limit. Keck is a 10 m large telescope. Its gravity deformation of M1 cell assembly and edge sensor errors due to cross coupling of motions and temperature will be calibrated by bright stars with known locations in the observable sky. Calibration of the dynamical characteristics is essential for the prediction of the response under wind distributions, mount slewing, and internal vibration from some translating and rotating components. GEMINI's resonance performance under wind load was estimated and calibrated with a dummy mirror and load cells [1–3].

Generally, when a telescope is pointing at a star with known location, the position of the telescope is known with a high degree of accuracy. However, the GSSM is a separately manufactured large plate, so additional equipment with adequate accuracy is required to fill up the lack of star calibration. The laser tracker is quite a convenient coordination metrology machine (CMM). The Giant Magellan Telescope (GMT), the 24 m segmented large telescope, has widely utilized it to measure, to align, and to locate large components. With two laser trackers, it is able to reach higher accuracy after cross calibration. VLTI and VISTA also processed metrology by laser trackers at the end of the 20th century to locate mirrors. For GSSM, a laser tracker will be used for calibration in very complex

working conditions where different zenith angles cross-coupled with tipping of the mirror, and the traditional methods (telescope, co-collimator, etc.) are not suitable [4–6].

Vibration may cause performance degradation. For large telescopes, it is common to be relatively soft due to limitation of mass, volume, and cost. GMT has flexible modes at just above 4 Hz. The large size of TMT results in resonance frequency as low as 2 Hz [7–9]. To cancel the effect of vibration, dynamical characteristics need to be previously measured. The 731A seismic accelerometer was used to measure the dynamical performance of GSSM. It incorporates an isolated piezoelectric sensing element that minimizes the effects of transverse motion, base strain, and thermal transients. After measurement, passive or active damping means are designed as add-on treatment, which has effectively reduced extremely tall buildings shaking in wind and jitter of the air-based telescope, SOFIA [10,11].

The warping harness technique, based on the three local degrees of freedom (DoF) of the hard points in a passive support system, introduces additional local DoFs through its own flexibility. It is called semi-active support. The warping harness is to be utilized in GSSM, correcting the gravity print, which is mainly dominated by primary Zernike polynomials [12].

GSSM is an extremely large system. To learn and understand, a 1/4-scale prototype will be under construction by Changchun Institute of Optics, Fine Mechanics, and Physics, Chinese Academy of Sciences. It is called the Giant Steerable Science Mirror prototype (GSSMP) [13–18].

This paper is organized as follows. Section 2 describes the GSSMP system, including the coordinate system and function of GSSMP. Section 3 presents the procedure of calibration. In Section 4, the added-on treatment is discussed after measurement of GSSMP dynamical resonance. In Section 5, the warping harness combining Zernike mode and bend mode is investigated.

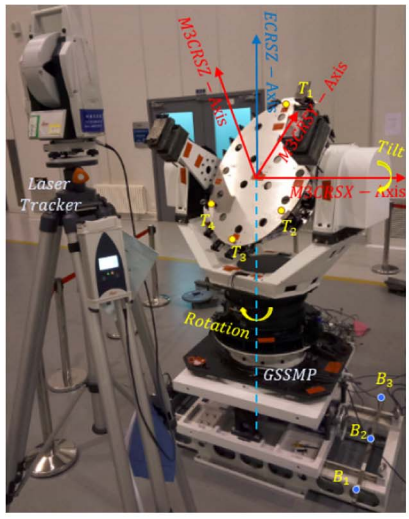

Fig. 1. GSSMP calibration, for (a) showing coordinate system and details of the assembly and for (b) results achieved by two SMRs and three SMRs.

2. DESCRIPTION OF GSSMP

The first thing that needs to be defined is the coordinate system of the GSSMP. All motions are about the z axis of the elevation coordinate system (ECRS) and the x axis of the M3 coordinate system (M3CRS). For the calibration, the goal is to precisely measure the difference between commanded and actual positions, and then to fine-tune the performance by means of control algorithms. In order to measure the actual position and check that all the motion requirements are fulfilled, a calibration lookup table that lists encoder reading errors was created [13,14].

For pointing and tracking, the M3 system (M3S) rotation range about the ECRS z axis will be within two ranges: $\theta = +14$ to -28 deg for instruments on the $+X$ Nasmyth Platform and $\theta = +166$ to $+208$ degrees for instruments on the $-X$ Nasmyth platform. For pointing and tracking, M3S will tilt about the M3CRS x axis within the range $\Phi = 32$ to 48 deg. Figure 1(a) shows the M3CRS.

The M3S will be able to rotate the M3 Mirror about the ECRS z axis to any angle within the ranges with a repeatable residual M3 rotation error (after telescope calibration) that is less than 3.5 arcsec RMS. The M3S will be able to tilt the M3 mirror about the M3CRS x axis to any angle within the range with a repeatable residual M3 tilt error (after telescope calibration) that is less than 3.5 arcsec RMS. The residual position error of the M3 mirror surface in the M3CRS z-axis direction will be less than 120 μm RMS (after telescope calibration) as the M3S rotates and tilts the M3 mirror to any position within the ranges defined before.

If possible, the following characteristics of the GSSMP system need calibration, including deformations due to gravity, encoder geometric errors after controlling of the encoder mounting surface quality to a good level, thermal effects after dome thermal control, structural repeatability under a changing thermal and gravitational environment, and cross-coupling between the rotation and tilt axes after alignment of orthogonality between tilt and rotation axes.

The tracking performance relates to the resonance of the GSSMP system and the control algorithm. The jitter requirement is easier to meet, when the added-on treatment is investigated. It will minimize the influence of jitter on the system performance. The location for these is on the yoke and the cell assembly, if necessary.

The warping harness will be rooted on the whiffletrees, which support the planar mirror. The mirror is sensitive to

bending, which can be used to adjust deflection due to gravity and thermal load.

3. GSSMP CALIBRATION

Motion calibration is mainly focused on pointing error. It will allow us to achieve the pointing performance with high accuracy, even though the encoder is imperfectly mounted or the control system is imperfectly tuned. It might be impossible to meet the requirement without calibration at a relatively low cost. Calibration is trying to figure out, mostly, how to remove the systematic error, which is stable over the timescale between calibrations. The temporal and/or spatial frequencies of the error components decide the type of calibration model. A suitable calibration model will help to predict the values of the error between sampled points using polynomial fit or sum of sines/cosines, etc.

The calibration is processed by a laser tracker and sphere-mounted retro-reflector (SMR). The SMR will feed back its location to the laser tracker. As shown in Fig. 1(a), the residual error curves of three SMRs and two SMRs are presented. The averaging of three and two SMRs is better than both of them. Analytically, three SMRs will constrain errors except components of three orders and their multiples. Averaging two and three SMRs will leave only t6 orders and their multiples. As shown in Fig. 1(b), the GSSMP will be calibrated at different Zenith angles, and the SMRs will be located on the dummy mirror.

The plot presents the pointing error of GSSMP. The bearing for the rotation axis was mounted correctly, and measurements of rotation were made with four SMRs. The data show that four read heads/SMRs cancelled run-out almost entirely. The residual error represents the true bearing error, which can be corrected in an algorithm to get extremely accurate readings. Angles tested at points $T_1 \sim T_4$ by four read heads/SMRs are set as $T_1 \sim T_4$. Rotation angle θ_{rot} is shown in Eq. (1):

$$\theta_{\text{rot}} = \frac{1}{2}\frac{R_2}{R_1+R_2}(T_1+T_3)+\frac{1}{2}\frac{R_1}{R_1+R_2}(T_2+T_4), \quad \textbf{(1)}$$

where $r_1 = r_3 = R_1$, and $r_2 = r_4 = R_2$. The accuracy is equal to the two reading heads case.

Here we chose the weights as $\frac{R_2}{R_1+R_2}$ for the test points T_1, T_3, and $\frac{R_1}{R_1+R_2}$ for the points T_2, T_4. Figure 2 shows schematically the principle of calibration. The bottom panel shows the raw data of four SMRs.

The purpose is to measure the pointing errors, testing used angle measurements from all four SMRs. However, only one read head is used to feed back to the control system. Residual run-out in the bearing is likely much larger than the four SMRs measurement, relatively. Here we note the averaging error as $\bar{\Delta}_i = \frac{\sum \Delta_i}{N} - \delta_{ai}$, and the difference between GSSMP encoder and reference encoder as $\Delta_i = \delta_{bi} - \delta_{ai}$, setting $\mu_i = \Delta_1 - \bar{\Delta}_i = \delta_{bi} - \frac{\sum \delta_{bi}}{N}$. Because $\frac{\sum \delta_{bi}}{N}$ is very close to being dominated by random error when N is large enough, μ_i is the asymptotic estimation of δ_{bi}.

The residual error of ration at 0 zenith is shown in Fig. 3(a). The residual error of tilt at 0 zenith is shown in Fig. 3(b).

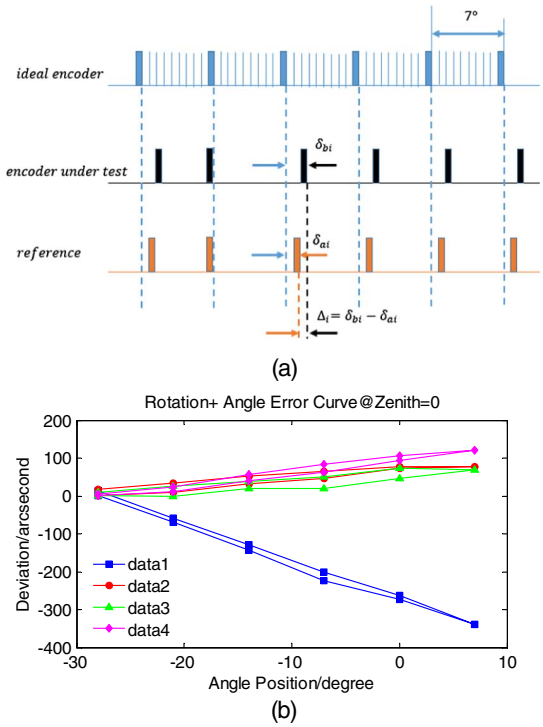

Fig. 2. Configuration of the calibration with a laser tracker for (a) basic principles and (b) raw data.

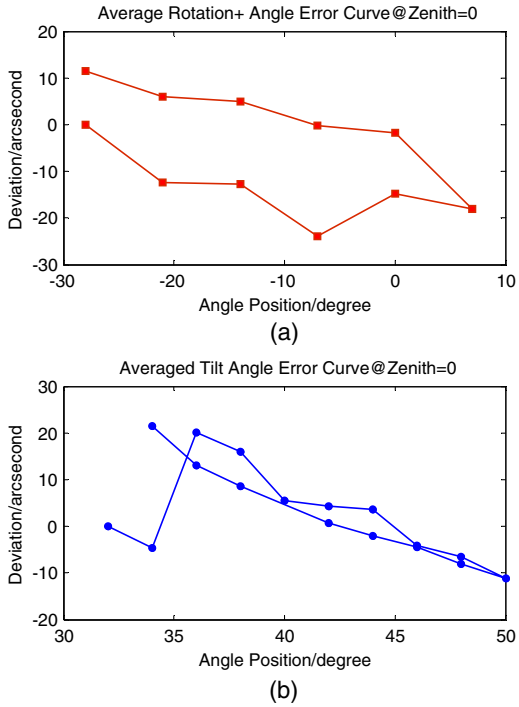

Fig. 3. Residual error of the calibration with a laser tracker for (a) rotation axis and (b) tilt axis.

This can work with a large correction table to include the run-out measurement for only one read head, but the correction values at any point are likely to be much larger than the

errors that the table is trying to eliminate. Static alignment terms (rotation offset, tilt offset, non-orthogonality between rotation axis and tilt axis, non-orthogonality between tilt axis and ECRS-z, etc.) are then discussed. As shown in Eq. (2), the rotation deviation $\Delta\theta$ and tilt deviation $\Delta\phi$ are presented:

$$\Delta\theta = -(b_1 \sin\theta - b_0 \cos\theta)\cot\phi - b_3 \csc\phi$$
$$\Delta\phi = -b_1 \cos\theta - b_2 \sin\theta, \tag{2}$$

where b_0 stands for rotation offset, b_1 stands for tilt offset, b_2 stands for non-orthogonal tilt and ECRS-z, and b_3 stands for non-orthogonal rotation-tilt.

By least squares estimation (LSE) estimation, the coefficient is rotation offset $|b_0| = 27.5''$, tilt offset $|b_1| = 26.31''$, non-orthogonal tilt and ECRS-z $|b_2| = 110.05''$, and non-orthogonal rotation-tilt $|b_3| = 102.91''$. The accuracy is better than $8''$. When it comes to the full-sized GSSM, the accuracy will be higher due to larger measurement diameter.

4. GSSMP TMD ANALYSIS

The input–output model is able to be evaluated in frequency or time domains. In time domain, it is evaluated by setting time, which is a one-dimension metric not enabling to specify the different components in the responses. In frequency domain, frequency response function (FRF) between input excitation and dummy mirror responses is investigated. In general, the lowest modes will dominate the responses. However, considering the coupling of telescope components, the higher-frequency modes may also become fundamental modes.

For GSSMP, the fundamental mode is a translation along tilt axis, as shown in Fig. 4. To modify the FRF of GSSMP, an additional treatment is set to the GSSMP, as shown in the far right panel of Fig. 4.

Tuned mass damping (TMD) is very effective for single-resonance modal shape. The very first step is the selection of potential mounting locations. The candidate principle is physical mounting restriction. On the top of the yoke, the light transition will not be influenced. Furthermore, it is easy to be assessed to replace and repair. By FRF measurement, the basic resonance characteristics of GSSMP will be illustrated. After that, based on FRF, the TMD is able to be designed to improve the dynamical performance of GSSMP.

The dynamical equation is shown in Eq. (3):

$$\begin{bmatrix} I_G & 0 \\ 0 & I_B \end{bmatrix}\begin{bmatrix} \ddot{\alpha} \\ \ddot{\theta} \end{bmatrix} + \begin{bmatrix} 2k_1 l_G & -2\cos(\varphi)k_1 l_G \\ -2\cos(\varphi)k_1 l_G & 2\cos(\varphi)k_1 l_G + 2kl_B \end{bmatrix}\begin{bmatrix} \alpha \\ \theta \end{bmatrix} = \begin{bmatrix} 2l_G m_{\mathrm{TMD}}\ddot{x}_{\mathrm{TMD}} \\ 0 \end{bmatrix}, \tag{3}$$

where I_G is the moment of inertia of GSSMP; I_B is the moment of inertia of GSSMP base; α is the angular displacement of GSSMP tipping; θ is the angular displacement of GSSMP base tipping; k_1 is the stiffness of GSSMP tipping; l_G is the arm of force in GSSMP; φ is the rotation angle of GSSMP; k is the stiffness of GSSMP base; l_B is the arm of force in GSSMP base; m_{TMD} is the mass of TMD; and x_{TMD} is the displacement of TMD.

Rewrite Eq. (3) in frequency domain, as shown in Eq. (4):

$$\begin{aligned}&(I_G\omega^2 + 2k_1 l_G)\mathrm{A}(\omega) \\ &\quad = 2\cos(\varphi)k_1 l_G\Theta(\omega) + 2l_G m_{\mathrm{TMD}}\omega^2 X_{\mathrm{TMD}}(\omega) \\ &[I_B\omega^2 + 2\cos(\varphi)k_1 l_G + 2kl]\Theta(\omega) \\ &\quad = -2\cos(\varphi)k_1 l_G\mathrm{A}(\omega),\end{aligned} \tag{4}$$

where $\mathrm{A}(\omega)$ is the Fourier transform of α; $\Theta(\omega)$ is the Fourier transform of θ; and $X_{\mathrm{TMD}}(\omega)$ is the Fourier transform of x_{TMD}.

The FRF between the angular displacement of GSSMP tipping and TMD force is shown in Eq. (5):

$$H = \frac{\mathrm{A}(\omega)}{m_{\mathrm{TMD}}\omega^2 X_{\mathrm{TMD}}(\omega)} = \frac{2l_G(I_B\omega^2 + 2\cos(\varphi)k_1 l_G + 2kl_B)}{(I_G\omega^2 + 2k_1 l_G)(I_B\omega^2 + 2\cos(\varphi)k_1 l_G + 2kl) + 4[\cos(\varphi)k_1 l_G]^2}. \tag{5}$$

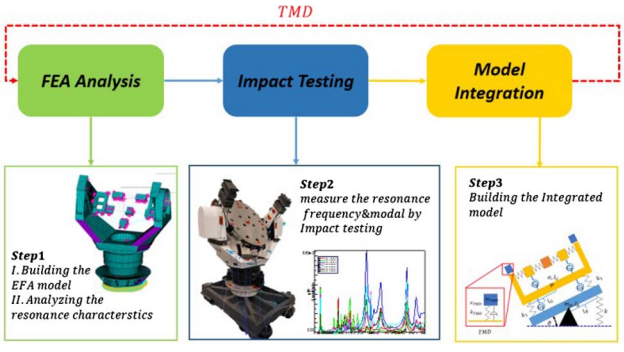

Fig. 4. GSSMP model and the sketch of TMD.

The derivative of FRF between the angular displacement of GSSMP tipping and TMD force is shown in Eq. (6). The derivative is positive; when $\varphi = 0$, GSSMP tipping is easier to be influenced by TMD:

$$\frac{\partial H}{\partial\cos(\varphi)} = \frac{\partial\frac{\mathrm{A}(\omega)}{m_{\mathrm{TMD}}\omega^2 X_{\mathrm{TMD}}(\omega)}}{\partial\cos(\varphi)} \geq 0. \tag{6}$$

The FRF will be tested by hammer impact or a mini actuator at $\varphi = 0$. The imaginary part of FRF $H = H^{\mathrm{REA}} + iH^{\mathrm{IMA}}$ is presented by stiffness, mass, and damping, as shown in Eq. (7):

$$H^{\mathrm{IMA}} = \frac{-1}{2k_{\mathrm{main}}\xi_{\mathrm{main}}} = \frac{-1}{2m_{\mathrm{main}}\omega_0^2\xi_{\mathrm{main}}}, \tag{7}$$

where m_{main} is the mass of the main vibration model. ω_0 is the resonance frequency of the main vibration model. k_{main} is the stiffness of the main vibration model. ξ_{main} is the damping ratio of the main vibration model. Re-write the Eq. (7) as Eq. (8):

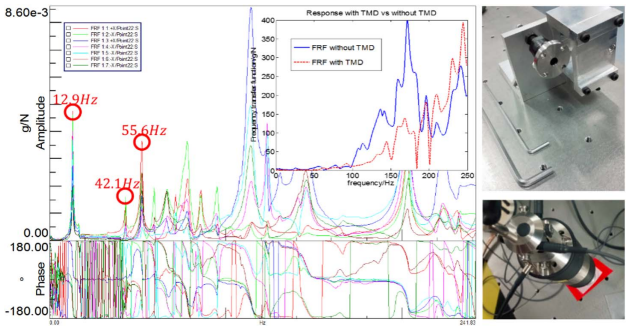

Fig. 5. GSSMP FRF and the TMD frequency performance.

$$m_{\text{main}} = \frac{-1}{2H^{\text{IMA}}\omega_0^2\xi_{\text{main}}}. \tag{8}$$

Considering the output is acceleration, $H_A^{\text{IMA}} = \omega_0^2 H^{\text{IMA}}$. The main mass is shown in Eq. (9); the mass of TMD is set as 2–5% of the main mass:

$$m_{\text{main}} = \frac{-1}{2H_A^{\text{IMA}}\xi_{\text{main}}}. \tag{9}$$

By this, the slewing setting time will be constrained. The FRF of GSSMP is shown in the left panel of Fig. 5. The resonance frequency of 12.9 Hz is according to rigid body motion. The peak of 42.1 Hz is the arm swinging from side to side. According to this model whose main mass is 210 kg, the TMD is designed. As shown in the left panel of Fig. 5, the mass of TMD is about 4 kg. What is more, the frequency is set as 42 Hz. The dynamical response was reduced by at least 20% in a previous testing, as shown in the right panel of 5. A mini actuator is shown in the right panel (lower), and it can be used in the reaching of FRF, but also as active mass damping items.

5. WARPING HARNESS

The biggest advantage of the stitching algorithm is the expansion of the measurement aperture. However, with the telescope diameter increasing, the number of subapertures will also increase. What is more, because subapertures are stitched together after extraction of low-order aberration (power, astigmatism, etc.), the measuring sensitivity is low for the lower frequencies. At the same time, the cost will be difficult to control, if a larger plane interferometer is used to increase the estimated accuracy. Additionally, measuring lots of apertures is a huge waste of time and staff. The sparse apertures were proposed to test the large flat mirror, combined with the theory of Fourier optics, and normalized point source sensitivity (PSSn). PSSn is an advanced large telescope error evaluation index proposed by the TMT team in the United States. Using point spread function (PSF) or optical transfer function (OTF), PSSn can be obtained under different seeing conditions. According to the Fourier optics theory, the difference between a sparse aperture and full aperture can be theoretically analyzed by PSSn.

The power spectral density (PSD) evaluation method is investigated by the National Ignition Facility (NIF) [19,20]. Armed with the fast Fourier transform, the PSD can be obtained rapidly. It is possible to estimate the low-order Zernike polynomials from the data of the sparse apertures.

The Zernike polynomial is the commonly used orthogonal basis optical surface expression. As Noll pointed out [21], in Eq. (10), it has a relationship between the Zernike coefficient and PSD:

$$\langle \bar{\alpha}_i \alpha_{j'} \rangle_{\Phi_{\text{sub}}} = \begin{cases} \frac{2\sqrt{n+1}\sqrt{n'+1}}{\pi R^2}(-1)^{(n+n'-m'-m)/2} \\ \times \int_{\vec{f}}^{\infty} \text{PSD}_s(\vec{f}/R)\frac{J_{n+1}(2\pi\vec{f})J_{n'+1}(2\pi\vec{f})}{\vec{f}}\,\mathrm{d}\vec{f} & i-j' = \text{even} \\ 0 & i-j' = \text{odd}. \end{cases} \tag{10}$$

Noting $J_n(2\pi\vec{f})$ as the n'th-order Bessel function of the first kind, n is the axial symmetry number, and m is the number of symmetry. a_i is the Zernike coefficient. m, n is integration. PSD_s is the power spectrum density achieved by sparse apertures. $\vec{f}$ is spatial frequency.

The power spectrum is a characterization method with statistical information that combines the frequency domain expression of Zernike polynomials to realize low-order face estimation. According to the continuity of functions, noting α_ϕ as the fitting coefficient, the RMS of the standard Zernike polynomial is 1, so the PSSn brought by a single Zernike is [22]

$$\text{PSSn} = 1 - \alpha_\phi k^2 \alpha_i^2.$$

And when only the first few orders are under consideration, it shown in Eq. (11):

$$\text{PSSn} \approx \prod_{i=2}^{N}(1 - 2k^2\alpha_i^2). \tag{11}$$

$k = \frac{2\pi}{\lambda}$ is the wave number, which is used for the optical path and phase transformation.

Combined with Zernike polynomials and minimum energy modes, the mirror figure can be expressed. The Zernike polynomial's biggest advantage is its direct meaning. At the same time, for a different system, its expression is unified. The minimum energy modes are obtained by modal calibration where the correction forces or torques are minimum. For different systems, due to the different free resonant modes, the bases will be different. TMT used the plate scale error to specify the low-order aberration. The definition and calculation method of the plate scale error are shown below:

$$E_{\text{PA}} = C_{\text{power}}\sqrt{\langle \alpha_4^2 \rangle_{\text{full}}} + C_{\text{astigmatisms}}\sqrt{\langle \alpha_5^2 \rangle_{\text{full}} + \langle \alpha_6^2 \rangle_{\text{full}}},$$

where

$$\begin{cases} C_{\text{power}} = |c_4@45° - c_4@32°| & = 1.97\ \text{mas/}\mu\text{mRMS} \\ C_{\text{astigmatisms}} = 2|c_5@45°| & = 63.70\ \text{mas/}\mu\text{mRMS} \end{cases}.$$

The advantage of combining Zernike modes with bending modes can be highlighted by the Zernike polynomial's aberration expression (plate scale error, etc.) and the bending mode's convenience in controlling.

Suppose the system wavefront is $W(\theta, \rho)$, and it is presented by Zernike polynomials $Z_j(\theta, \rho)_{j=2\sim6}$, which characterize the

system performance. Another base is obtained by bending modes $B_i(\theta,\rho)_{i=1\sim N}$, β_i is its coefficient.

Note that θ, ρ are the polar angle and polar radius under the polar coordinate.

$W(\theta,\rho)$ is expressed in Eq. (10). $W_{\text{res}}(\theta,\rho)$ is the residual wavefront error:

$$W(\theta,\rho)=\sum_{j=2}^{6}\alpha_j Z_j(\theta,\rho)+\sum_{i=1}^{N}\beta_i B_i(\theta,\rho)+W_{\text{res}}(\theta,\rho). \tag{12}$$

System wavefronts $W(\theta,\rho)$ and $B_i(\theta,\rho)_{i=1\sim N}$ can both be represented by Zernike polynomials:

$$W(\theta,\rho)=\sum_{k=2}^{K}\eta_k Z_k(\theta,\rho),$$

and

$$\beta_i(\theta,\rho)=\sum_{l=2}^{L}\gamma_k Z_l(\theta,\rho).$$

Combine with the previous equations:

$$\sum_{k=2}^{M}\eta_k Z_k(\theta,\rho)=\sum_{j=2}^{7}\alpha_j Z(\theta,\rho)+\sum_{i=1}^{N}\beta_i\sum_{l=2}^{L}\gamma_l Z_l(\theta,\rho). \tag{13}$$

Since Zernike polynomials are linearly independent, the corresponding coefficients are equal to Eq. (14):

$$\eta_k=\alpha_k+\sum_{i=1}^{N}\beta_i\gamma_k \qquad k=2\ldots7, \tag{14}$$

and

$$\eta_k=\sum_{i=1}^{N}\beta_i\gamma_k \qquad k\geq 8.$$

Reforming Eq. (14), it is Eq. (15):

$$\mathrm{A}=\begin{bmatrix}\alpha_1\\ \vdots\\ \alpha_7\end{bmatrix}=\begin{bmatrix}1&0&\cdots&0&-\gamma_1&\ldots&-\gamma_1\\ 0&1&\cdots&0&-\gamma_2&\ldots&-\gamma_2\\ \vdots&\vdots&1&0&\vdots&\ldots&\vdots\\ 0&0&\ldots&1&-\gamma_7&\ldots&-\gamma_7\end{bmatrix}\begin{bmatrix}\eta_1\\ \vdots\\ \eta_K\\ \beta_1\\ \vdots\\ \beta_L\end{bmatrix}=G\mathrm{B}. \tag{15}$$

Using the LSE method, the correction torques can be obtained:

$$\mathrm{B}=G^{+}\mathrm{A}.$$

The aberration is presented in the form of PSSn by Eq. (11). The complex amplitude distribution of a multi-aperture system is shown in Eq. (16):

$$I_A=\left|\frac{\pi D(1+\cos\theta)}{\lambda}\right|^2\left|\frac{J_1\left(\frac{\pi D\sin\theta}{\lambda}\right)}{\frac{\pi D\sin\theta}{\lambda}}\right|A, \tag{16}$$

where $\tan\theta=\frac{\sqrt{\xi^2+\eta^2}}{z}$, and (ρ_i,δ_i) are the polar coordinates of the subaperture array. $A=|\sum_{i=1}^{N}e^{j2\pi(\rho_i\theta/\lambda)\cos(\delta_i)}e^{j\phi_i}|^2\phi_i$ is the phase deviation of the ith subaperture. The complex amplitude at different locations is PSF. PSF gained by sparse aperture is similar to the single diameter case, but its internal part has more ripples. It can be seen from Eq. (16) that PSSn of the system can also change with the optics aperture. In the most extreme case, PSSn will reduce to 0, when the light no longer passes, and PSSn is limited by the optical pupil's shape. By estimating the upper limit, it is of great significance for the installation of PSSn. In order to demonstrate the universality of the conclusion for the limits of the sparse aperture's PSSn, we have calculated the surface data of various vendors. Considering different vendors, the PSSn limit is shown in Fig. 6(a). With a smaller filling ratio, due to the shrinking of effective information, PSSn will responsibly reduce, as shown in Fig. 6(b).

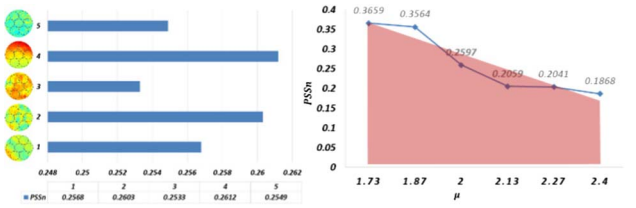

Fig. 6. PSSn limit showing for (a) PSSn with samples of different vendors, and for (b) PSSn for different sampling forms.

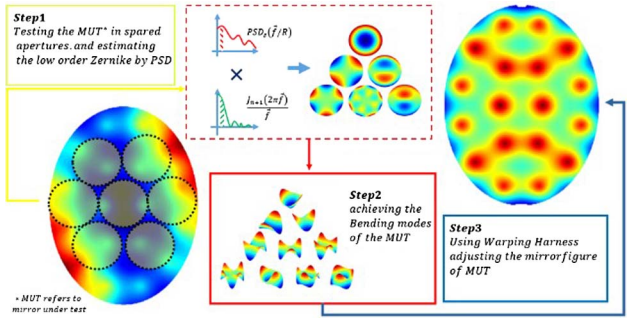

Fig. 7. Warping harness working process for GSSMP.

Using PSSn and sparse apertures as the feedback of warping harness correction is shown in Fig. 7. The first few Zernike polynomials were estimated in the frequency domain, and then PSSn was calculated. The warping harness was driven by the bending modes. The previous process was repeated until the PSSn was raised to the expected value. Last, PSSn increased from 0.1654 to 0.2548. The RMS value was improved from 78.9 nm to 23.4 nm. The correction rate reached 60%.

6. CONCLUSIONS

Calibration is a method for improving telescope pointing performance. At the same time, damping treatment is employed as an added-on solution for dynamical resonance improvement. Calibration by a laser tracker and non-uniformly located SMRs will reduce the systematic ration/tilt error, and feed back to the control system. The accuracy was better than 8″. When it comes to the full-sized GSSM, the accuracy will be higher due

to a larger measurement diameter. Dynamical performance depends on damping of the telescope very much. However, the main material of a large telescope is always lightly damped, such as steel. The added-on treatment is necessary not only for the design of future telescopes but also valuable for the reconstruction of current telescopes. The dynamical response was reduced by at least 20% in a previous testing. Using the figures in sparse apertures, we can obtain a system's partial information, which is needed for the system installation and the controlling of the warping harness. The sparse apertures were used to measure the non-overlapping figure, and then PSSn was estimated. With the warping harness, PSSn was increased from 0.1654 to 0.2548. The RMS value of the GSSMP mirror figure was improved from 78.9 nm to 23.4 nm. The correction rate reached 60%.

Funding. Youth Innovation Promotion Association of the Chinese Academy of Sciences (2016198); National Natural Science Foundation of China (NSFC) (11403022, 11673080).

Acknowledgment. The author is very grateful to Dr. Hong-chao Zhao for providing valuable suggestions and help, and thanks the TMT group for the use of their equipment and technology support.

REFERENCES

1. G. Z. Angeli, S. Roberts, and K. Vogiatzis, "Systems engineering for the preliminary design of the Thirty Meter Telescope," Proc. SPIE **7017**, 701704 (2008).
2. S. Roberts, J. Rogers, H. Thompson, K. Vogiatzis, and D. MacMartin, "Systems engineering of the Thirty Meter Telescope for the construction phase," Proc. SPIE **9150**, 91500V (2014).
3. N. Samantaray, I. R. Berchera, A. Meda, and M. Genovese, "Realization of the first sub-shot-noise wide field microscopeand solution concentration measurement," Light Sci. Appl. **6**, e17005 (2017).
4. S. Rudoler, O. Hadar, M. Fisher, and N. S. Kopeika, "Image resolution limits resulting from mechanical vibrations. Part 2: experiment," Opt. Eng. **30**, 577–589 (1991).
5. O. Hadar, I. Dror, and N. S. Kopeika, "Image resolution limits resulting from mechanical vibrations. Part IV: real-time numerical calculation of optical transfer functions and experimental verification," Opt. Eng. **33**, 566–578 (1994).
6. Y. Bao, X. Yi, Z. Li, Q. Chen, J. Li, X. Fan, and X. Zhang, "A digitally generated ultrafine optical frequency comb for spectral measurements with 0.01-pm resolution and 0.7-μs response time," Light Sci. Appl. **4**, e300 (2015).
7. T. M. Herbst, "Lessons for ELTs from the Large Binocular Telescope," Bull. Societé Royale des Sciences de Liège **74**(5–6), 435–443 (2005).
8. D. Mancini, M. Brescia, E. Cascone, and P. Schipani, "Variable structure control law for telescope pointing and tracking," Proc. SPIE **3086**, 72–84 (1997).
9. M. Schöck, T. Do, B. L. Ellerbroek, L. Gilles, G. Herriot, L. Meyer, R. Suzuki, L. Wang, and S. Yelda, "Thirty Meter Telescope astrometry error budget," Proc. SPIE **9148**, 91482L (2014).
10. H. J. Kaercher, "Evolution of the SOFIA Telescope system design: lessons learned during design and manufacturing," Proc. SPIE **4857**, 257–265 (2003).
11. J. R. Maly, P. J. Keas, and R. M. Glaese, "Damping SOFIA: passive and active damping for the stratospheric observatory for infrared astronomy," Proc. SPIE **4331**, 60–71 (2001).
12. M. Cayrel, "E-ELT optomechanics: overview," Proc. SPIE **8444**, 84441X (2012).
13. F. Yang, G. Liu, Q. An, and X. Zhang, "Method of evaluation of a mirror surface figure based on frequency domain and its application for the giant steerable science mirror of the Thirty Meter Telescope," Chin. Opt. Lett. **13**, 041201 (2015).
14. F. Yang, H. Zhao, P. Guo, Q. An, and H. Jiang, "Pre-construction of giant steerable science mirror for TMT," Proc. SPIE **9573**, 95730T (2015).
15. L. Han, J. Zhang, F. Yang, and Q. An, "Estimation of the GSSM calibration error," Appl. Opt. **55**, 8884–8892 (2016).
16. Q. An, J. Zhang, F. Yang, and H. Zhao, "Normalized point source sensitivity analysis in GSSM prototype," Chin. Opt. Lett. **15**, 111202 (2017).
17. F. Yang and Q. An, "The evaluation and analysis of mirror seeing based on PSSn," Opt. Precis. Eng. **24**, 979–985 (2016).
18. F. Yang, Q. An, J. Zhang, H. Zhao, P. Guo, and H. Jiang, "Seeing metrology of large aperture mirror of telescope," Opt. Precis. Eng. **25**, 2572–2579 (2017).
19. D. M. Aikens, C. R. Wolfe, and J. K. Lawson, "Use of power spectral density (PSD) functions in specifying optics for the National Ignition Facility," Proc. SPIE **2576**, 281–292 (1995).
20. M. L. Spaeth, K. R. Manes, C. C. Widmayer, W. H. Williams, P. K. Whitman, M. A. Henesian, I. F. Stowers, and J. Honig, "The National Ignition Facility wavefront requirements and optical architecture," Proc. SPIE **5341**, 25–42 (2004).
21. R. J. Noll, "Zernike polynomials and atmospheric turbulence," J. Opt. Soc. Am. **66**, 207–211 (1976).
22. B.-J. Seo, C. Nissly, M. Troy, G. Angeli, R. Bernier, L. Stepp, and E. Williams, "Estimation of normalized point-source sensitivity of segment surface specifications for extremely large telescopes," Appl. Opt. **52**, 4111–4122 (2013).